COMMUNICATION

Two-Inch-Sized Perovskite CH₃NH₃PbX₃ (X = Cl, Br, I) Crystals: Growth and Characterization

Yucheng Liu, Zhou Yang,* Dong Cui, Xiaodong Ren, Jiankun Sun, Xiaojing Liu, Jingru Zhang, Qingbo Wei, Haibo Fan, Fengyang Yu, Xu Zhang, Changming Zhao, and Shengzhong (Frank) Liu*

Semiconductor materials with a perfectly aligned lattice structure offer the best performance, not only in integrated circuits but also in photovoltaics and optoelectronics, etc. It is the invention of growth techniques for large-sized single crystals that has led to the birth of modern electronics, solar cells, solid-state lasers, light emitting diodes (LEDs), and so on. For example, for well-studied silicon (Si)-based solar cells, efficiency ranks in the order of single-crystalline Si > multicrystalline Si > microcrystalline Si > amorphous Si.[1] Likewise, high-efficiency GaAs-based solar cells need to use defect free epitaxial film, as do high-performance LEDs.

The organic–inorganic hybrid perovskite CH₃NH₃PbX₃ (X = Cl, Br, I) has emerged as a strong competitor in photovoltaic and general optoelectronic applications due to its superior characteristics including high absorption coefficient, direct bandgap, long carrier lifetime, and high balanced hole and electron mobility, etc.[2,3] In fact, the National Renewable Energy Laboratory (NREL) certificated power conversion efficiency for the perovskite solar cell has reached 20.1%.[1] However, until now, all perovskite solar cells have been based on microcrystalline and amorphous components, limited by the unavailability of large, single-crystalline material. As there are plenty of grains, boundaries, voids, and surface defects within the perovskite material, it is expected that significant efficiency losses will be seen, caused by these recombination sites. In fact, it is found that grain boundaries create electron trap states, leading to J–V hysteresis and reduced photovoltaic performance.[4–6] Recently, two separate research groups reported very low trap density in the single-crystalline perovskites, on the order of only 10^9 cm^{-3} to 10^{10} cm^{-3}, the same order as in single-crystalline Si, while it

is five orders of magnitude lower than that in microcrystalline perovskite. Consequently, the carrier mobility in single-crystalline perovskites is increased to 164 ± 25 cm^2 V^{-1} s^{-1} and diffusion length to 175 ± 25 µm[7] (while they are lower in another report: 115 cm^2 V^{-1} s^{-1} for carrier mobility and 10 µm for the diffusion length.[8] More importantly, the light absorption onset shifts to 820 nm, allowing the theoretic current density to be increased to 33 mA cm^{-2} for the crystalline perovskite. It is envisaged that solar cells made of single-crystalline perovskite will render significantly higher power conversion efficiency, as it offers not only better carrier generation and transport efficiencies, but also a broader light-absorption spectrum. Moreover, the stability of single-crystalline perovskite is expected to be better than its microcrystalline counterparts with a larger amount of inclusions and adsorbates.

Unfortunately, it is always challenging to grow a large-sized single-crystalline material. Only very recently, millimeter-sized perovskite crystals are being reported,[7–9] with the largest crystal size limited to about 10 mm. By using ion convection in a precursor solution, Huang and co-workers developed a top-seed solution growth (TSSG) method to prepare single-crystalline perovskite on a piece of silicon substrate. In the process, smaller perovskite crystals synthesized in advance separately were used as the seed to grow into an average size of 3.3 mm and the largest size was ≈10 mm.[7] Bakr and co-workers reported their antisolvent vapor diffusion process to harvest millimeter-sized CH₃NH₃PbBr₃ and CH₃NH₃PbI₃ perovskite single crystals.[8] On the other hand, by slowly decreasing temperature from 65 °C to 40 °C to induce saturation of the solute, in about a month of growth period, Tao and co-workers harvested single-crystalline CH₃NH₃PbI₃ with the largest size 10 mm × 10 mm × 8 mm.[9]

For commercial applications, larger crystals with dimension in inches are needed. All of the above three methods are still too time consuming to meet the large-scale production requirements. In this regard, we developed a facile method to prepare two-inch-sized perovskite crystals with high crystalline quality. In addition to CH₃NH₃PbI₃, similar techniques have been adopted to grow inch-sized CH₃NH₃PbBr₃ and CH₃NH₃PbCl₃ crystals. It is found that crystal growth rate is proportional to the total surface area of the seed crystal. By carefully analyzing the shape-evolution process, we propose a seed-induced heterogeneous nucleation mechanism to explain the crystal-growth process. The largest crystal produced so far is 71 mm × 54 mm × 39 mm, to the best of our knowledge, this is the first time to report this type of perovskite crystals with dimensions exceeding half an inch. The X-ray 2θ measurement of the

Y. Liu, Dr. Z. Yang, D. Cui, X. Ren, J. Sun, X. Liu,
J. Zhang, Prof. Q. Wei, Prof. H. Fan, F. Yu, X. Zhang,
C. Zhao, Prof. S. (F.) Liu
Key Laboratory of Applied Surface
and Colloid Chemistry
National Ministry of Education, Institute for
Advanced Energy Materials, School of Materials
Science and Engineering
Shaanxi Normal University
Xi'an 710119, P. R. China
E-mail: zyang@snnu.edu.cn; szliu@dicp.ac.cn
Prof. S. (F.) Liu
Dalian Institute of Chemical Physics
Dalian National Laboratory for Clean Energy
Chinese Academy of Sciences
Dalian 116023, P. R. China
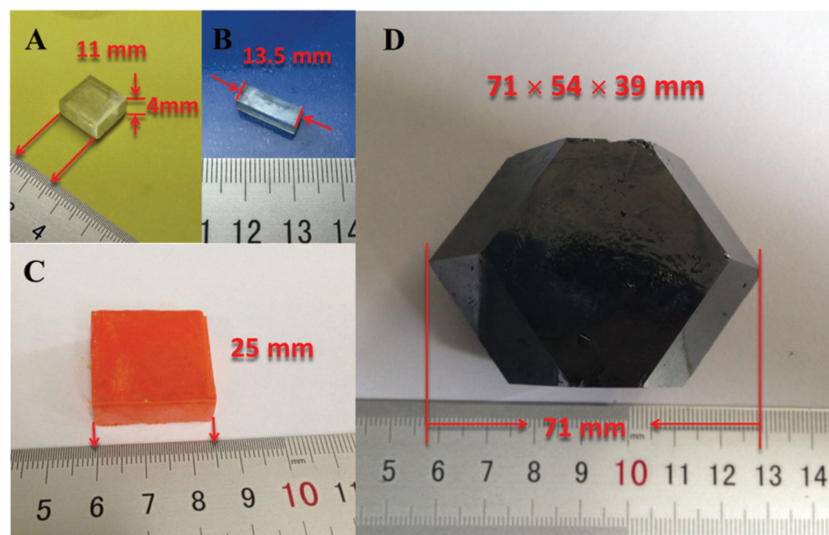
Figure 1. Photographs taken from the as-grown CH$_3$NH$_3$PbX$_3$ crystals, A,B) X = Cl, 11 mm × 11 mm × 4 mm and 13.5 mm × 13.5 mm × 4.5 mm; C) X = Br, 25 mm × 25 mm × 6 mm; D) X = I, 71 × 54 × 39 mm.

crystal shows only diffraction peaks from the (200) and (400) planes, indicating that it is indeed a single crystalline. The rocking curve measurement shows a strong peak at 10.2°, corresponding to the (200) diffraction peak in the 2θ scan mode. The full width at half maximum (FWHM) of the peak is measured 0.3718°, indicating that it is a single crystal with respectable crystalline quality. It is worthwhile pointing out that the rocking curve data are the very first report of an inorganic–organic hybrid perovskite to our knowledge.

Figure 1 shows photographs of a few representative perovskite (CH$_3$NH$_3$PbX$_3$ (X = Cl, Br, I)) crystals (more different size single-crystal images shown in Figure S1, Supporting Information). It is interesting to see that the CH$_3$NH$_3$PbCl$_3$ crystals are clear in color and cuboid in shape (Figure 1A,B). A similar shape is observed for the CH$_3$NH$_3$PbBr$_3$ crystals while they become orange color (Figure 1C). Figure 1D shows one typical CH$_3$NH$_3$PbI$_3$ crystal. While most of them are generally formed as dodecahedrons, some exhibit facets consistent with rhombo-hexagonal dodecahedrons, a typical crystal habit of a body-centered tetragonal lattice, in agreement with the reported structure at room temperature.[10] The different crystal shapes are commonly caused by intrinsic crystallographic structures and preferred growth directions.

To understand the growth mechanism of the perovskite crystals, we carefully studied the evolution process of the CH$_3$NH$_3$PbI$_3$ crystal from its initial nucleation to the development process into large single crystals.

To grow large single-crystalline CH$_3$NH$_3$PbI$_3$, CH$_3$NH$_3$I and PbI$_2$ were mixed and dissolved into gamma-butyrolactone (GBA) as the precursor solution. Small perovskite particulates, with diameter ≈ 2 mm, were harvested as seed crystals by keeping 20 mL of precursor solution at 100 °C for 24 h. By placing a seed crystal in 20 mL of precursor solution and keeping it at 100 °C for 48 h, the seed grew into a larger perovskite crystal with ≈7 mm in length. To prepare larger crystals, the above step is repeated, except that the large crystal is used

as the new seed. By repeating the process, larger and larger crystals are produced.

It is found that in the temperature range from 80 °C to 100 °C, the higher the temperature, the faster the crystals grow. However, when the temperature is increased to above 100 °C, the higher temperature leads to irregular shapes and stacked together. It should be pointed out that these single crystals can be re-dissolved into solution if the small crystals are kept in the solution at room temperature for an extended period of time, indicating that the crystal-growth process is reversible. The seed crystal provides a heterogeneous nucleation site, on which an additional crystalline layer grows faster than it is formed in solution.

Figure 2 shows photos of the crystal growth with and without seed crystal for 12 h. It is clear that without a seeding crystal, in Figure 2-A1, after 12 h, about 250 small (≈1.5 mm) crystals were formed, most precipitated along the edges of the glass slide underneath (Figure 2-A2). When a 6 mm crystal was used as the nucleation seed (Figure 2-B1), it grew into an 11 mm crystal in 12 h at 100 °C (Figure 2-B2). In addition, there were about 50 smaller crystals (1–2 mm) formed along the glass-slide edges, as the sharp edge of the glass slides provides nucleation sites for the perovskite crystal growth. By increasing the seed to 13 mm (Figure 2-C1), a larger crystal with length 23 mm was harvested (Figure 2-C2). Further increasing the size of the seed crystal to 22 mm, a 28 mm crystal was produced in the same length of time (Figure 2-D1, D2). Note that, for comparison, all crystal sizes mentioned are quantified using the diagonal length of the crystals. Apparently, the perovskite crystal seed appears to be a preferential site for the crystal growth. **Table 1** shows the diagonal length, surface area, volume of the initial crystal, and that of the final one after 12 h of growth. It is apparent that the larger the seed, the faster the growth rate (Figure S2, Supporting Information). **Figure 3** shows the final crystal volume (proportional to the mass of the crystals) as a function of surface area of the initial seed crystal. It is surprising to see that the linear correlation is so pronounced with $R^2 > 0.99$, in other words, the crystal growth rate follows a first-order mechanism to the seed surface area.

As expected, the precursor solution is found to play an important role in the growth process. When its concentration was lower than 0.5 M, the seed crystal was dissolved into the solution, revealing that the crystallization–dissolution process is reversible. In other words, when the solution is over-saturated, crystallization dominates; while the concentration is too low, the dissolution becomes more visible and the seed crystal would dissolve into the solution. Meanwhile, when the concentration was raised to 2 M, the product crystal surface became irregular; further increase of the concentration would form multiple smaller crystals attached to each other. By systematically optimizing the solution concentration, it is found that for the reaction condition used, the optimal concentration is at [CH$_3$NH$_3$PbI$_3$] ≈ 1.23 M.
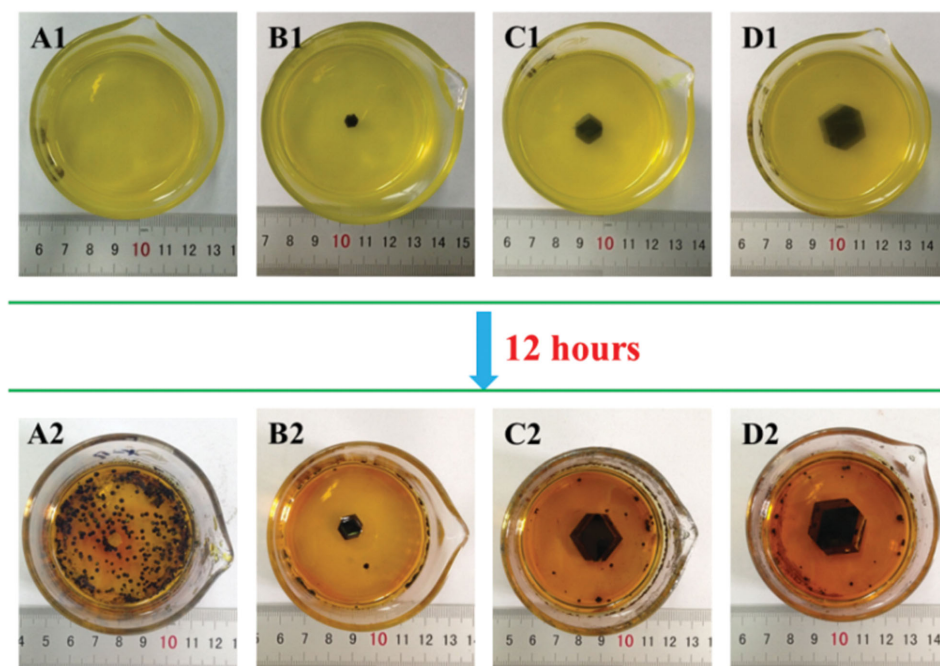
Figure 2. Photograph of the crystal growth for 12 h. A1. Clear precursor solution without seed. A2. The A1 after 12 h of growth at 100 °C. The B1, C1, and D1 are photos at initial stage when the seed crystal is placed into the fresh precursor solution. The B2, C2, and D2 are photos of the B1, C1, and D1 after 12 h of growth at 100 °C.

Moreover, the solvent is an important part as well. With limited optimization using 3 common solvents, namely GBA, N,N-dimethylformamide (DMF), and dimethylsulfoxide (DMSO), it is found that GBA works best for $CH_3NH_3PbI_3$. Not only that GBA offers enough solubility to raw materials PbI_2 and CH_3NH_3I, it seems to dissolve nanoparticles of the $CH_3NH_3PbI_3$ material to form large single crystals with clean facets. However, we failed to grow good single crystals of $CH_3NH_3PbBr_3$ or $CH_3NH_3PbCl_3$ using GBA in the limited experimental space explored. It was found that the optimal solvent for $CH_3NH_3PbBr_3$ is DMF, and DMSO works best for the $CH_3NH_3PbCl_3$.
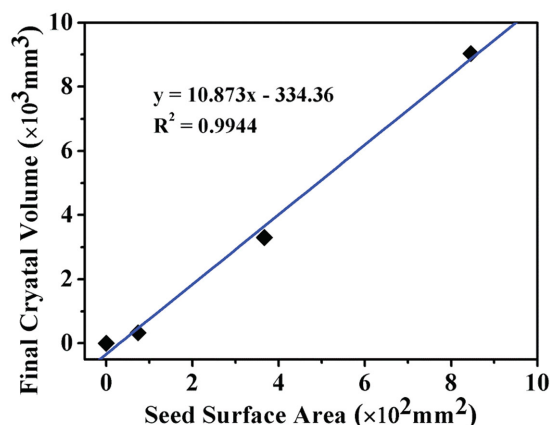
X-ray diffraction (XRD) is a powerful tool to characterize quality of crystalline materials. **Figure 4** shows XRD of small $CH_3NH_3PbX_3$ (X = Cl, Br, I) perovskite particulates ground from a piece of corresponding large crystal. In order to make sure that the samples are free from residues or inclusion of starting materials CH_3NH_3X and PbX_2, the XRD from the reactant samples was also measured and is included in Figure 4A–C. Careful examination confirms that there is no

crystalline residue from either CH_3NH_3X or PbX_2 in the final crystal products. All the samples are not only pure in composition, but also in crystalline phases.

Powder XRD crystallographic analysis reveals that the crystal structure of the $CH_3NH_3PbCl_3$ perovskite belongs to the cubic system (space group $Pm\overline{3}m$, $a = b = c = 5.6855$ Å) at room temperature (Figure 4A), similar to that reported in the literature.[11,12] The powder XRD of the single-crystalline $CH_3NH_3PbBr_3$ (Figure 4B) shows diffraction peaks at 14.9, 21.28, 30.2 corresponding to the (100), (110), (200) lattice planes of the cubic structure (space group $Pm\overline{3}m$, $a = b = c = 5.9171$ Å) at room temperature, consistent with the results reported by using powdered sample.[8,13–20] For X = I (Figure 4C), the powder XRD shows the formation of a tetragonal structure at room temperature, by fitting the powder XRD patterns, the unit cell parameters are determined $a = b = 8.8725$ Å, $c = 12.547$ Å, which is perfectly assigned to an $I4/m$ space group, in agreement with that reported in the literature for powder samples.[7,8,10,13,21,22] Meanwhile, the clear spilt of the (220) and (004) peaks (tagged in Figure 4C) further confirms that the

Table 1. The diagonal length, surface area, volume of the initial seed crystal, and the final grown crystal after 12 h growth.

	Initial				After 12 h		
Side length [mm]	Diagonal length [mm]	Surface area [mm²]	Volume [mm³]	Side length [mm]	Diagonal length [mm]	Surface area [mm²]	Volume [mm³]
0	0	0	0	1	1.5	6	2
5	6	74	56.5	8	11	254	325
11	13	367	619	21	23	989	3296
19	22	846	2282	23	28	1624	9033

Materials
Views
www.MaterialsViews.com

ADVANCED
MATERIALS
www.advmat.de

COMMUNICATION

**Figure 3.** The final crystals volume as a function of surface area of the initial seed crystals.

as-grown crystal adopts a tetragonal phase[10,16] with high crystalline quality.

For comparison, XRD patterns of the three perovskite crystals are shown in Figure 4D. It shows that main peaks for the

$CH_3NH_3PbI_3$ are at $2\theta = 14.1°$, $28.4°$, $31.9°$, for $CH_3NH_3PbBr_3$ at $14.9°$, $30.2°$, $33.9°$, and for $CH_3NH_3PbCl_3$ at $15.6°$, $31.5°$, $35.3°$. It is clear that all three major peaks shift higher from I to Br to Cl, indicating that the lattice spacing decreased as expected.

High-resolution X-ray diffraction was used to examine the quality of the single-crystalline $CH_3NH_3PbI_3$ perovskites. Figure S3 (Supporting Information) shows the 2θ scan results with only diffraction peaks from the (200) and (400) planes, demonstrating its single-crystalline nature. The rocking-curve measurement shows a strong peak at $10.2°$, corresponding to the (200) diffraction peak in the 2θ scan mode. The FWHM of the peak is measured $0.3718°$, indicating that it is a single crystal with respectable crystalline quality. It is worthwhile pointing out that the rocking-curve data are the first report on an organic–inorganic hybrid perovskite.

The optical properties of the as grown crystals were investigated using UV–vis–NIR and photoluminescence (PL) spectrometers. **Figure 5**A shows the (UV–vis–NIR) absorbance spectra for the $CH_3NH_3PbX_3$ (X = Cl, Br, I) perovskites. It is clear that the substitution from Cl to Br to I leads to dramatic changes in absorbance. The absorption onsets shift
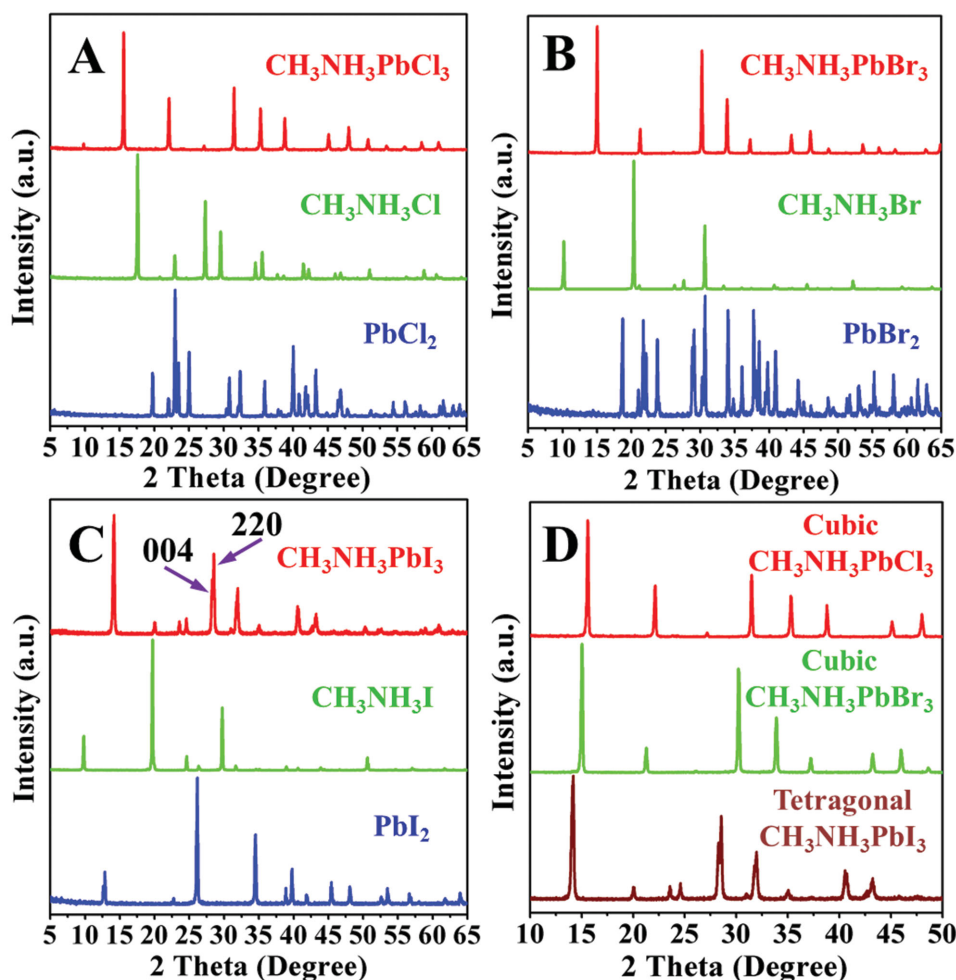
Figure 4. X-ray diffraction patterns of the ground powder from large $CH_3NH_3PbX_3$ single crystals, A) X = Cl, B) X = Br, C) X = I, D) the XRD comparison of three perovskites.
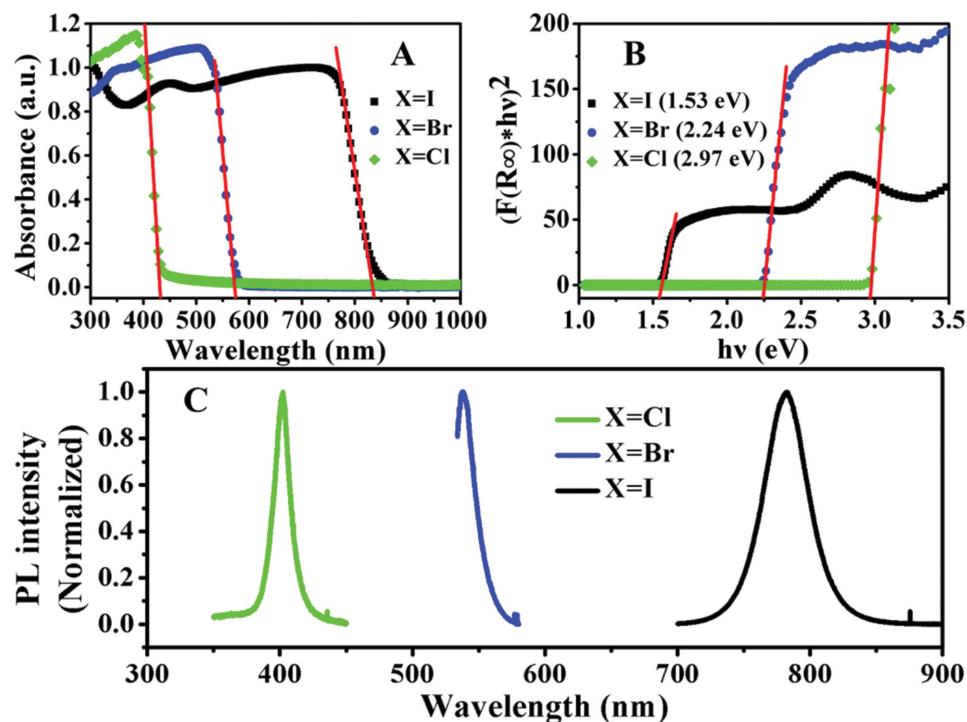
Figure 5. UV–vis–NIR absorption spectrum, bandgap determination, and photoluminescence (PL) properties of $CH_3NH_3PbX_3$ (X = Cl, Br, I): A) absorption spectrum, B) bandgap, C) photoluminescence spectrum.

from 431 nm for Cl to 574 nm for Br and to 836 nm for I. All spectra show clear band edge cutoffs with no excitonic signature or absorption tails, indicating high-quality crystals with low defect concentration. The $CH_3NH_3PbCl_3$ is very transparent in the visible spectrum, showing strong absorbance only in the very short-wavelength region. The $CH_3NH_3PbBr_3$ is orange in color, with absorption starting from ≈570 nm. In comparison, the $CH_3NH_3PbI_3$ shows strong absorption across the entire visible spectrum and therefore it is seen as black in color, as shown in Figure 1. The bandgap value was obtained on the basis of the Tauc plot as the intercept value of the plot of $(\alpha h\nu)^{1/m}$ or $(F(R_\infty)h\nu)^{1}/m$ against light energy ($h\nu$). As all three kinds of $CH_3NH_3PbX_3$ are direct-bandgap semiconductor materials, the m value is 1/2.[23] By extrapolating the linear region of the $(F(R_\infty)h\nu)^2$ to the energy-axis ($h\nu$) intercept[24] as shown in Figure 5B, E_g is established. The optical properties as a function of the halogen anions (and their ionic radius[25]) are summarized in **Table 2**. It is clear that the bandgap energy is reduced by increasing the ionic radius of the halogen anion in the $CH_3NH_3PbX_3$ (X = Cl, Br, I) perovskite. It is determined that the $CH_3NH_3PbI_3$ gives a bandgap of 1.53 eV, which is very

consistent with prior measurements on powder material.[26] The $CH_3NH_3PbBr_3$ and $CH_3NH_3PbCl_3$ present larger bandgaps 2.24 and 2.97 eV, respectively, both are significantly smaller than the values measured using their corresponding thin-film counterparts.[27] It should be noted that all the above bandgap values from Figure 5B show that the large crystals exhibit substantially narrower bandgaps than their corresponding microcrystalline and thin-film material,[22,27–30] or more extended optical absorption into longer-wavelength region. Figure 5C shows the PL spectra of the perovskite: $CH_3NH_3PbCl_3$, $CH_3NH_3PbBr_3$, and $CH_3NH_3PbI_3$, exhibiting narrow PL peaks at ≈402, ≈537, and ≈784 nm, respectively. Table 2 lists the absorption onset and corresponding PL peak values. It is interesting to see that the PL peak values of all three perovskites are smaller than the absorption onsets, implying that the lights of PL due to the excitation can be extinguished by themselves. There is no doubt that it is advantageous for them to be applied in solar cells. The blue-shifted and narrower PL peak also indicates a lower trap density in the material.[19] Considering that it has been reported repeatedly by different groups[26,27] that no PL emission is observed from solution-grown $CH_3NH_3PbCl_3$ nanocrystalline material at room temperature, the PL appears to be much more prominent in the present single-crystalline samples. As far as we know, this is the first time to observe a strong PL emission peaked at ≈402 nm from the $CH_3NH_3PbCl_3$ samples. We attribute it to the high-quality material and appropriate excitation applied using the 325 nm laser source.

To examine the thermal stability of the perovskite $CH_3NH_3PbX_3$ (X = Cl, Br, I) systems, thermogravimetric analysis (TGA) was carried out under nitrogen flow from room temperature to 800 °C as shown in **Figure 6**. For comparison, TGA

Table 2. Optical properties of $CH_3NH_3PbX_3$ single-crystalline samples as a function of the anions.

X	Ionic radius [Å]	λ_{onset} [nm]	E_g [eV]	PL peak [nm]
Cl	1.81	431	2.97	402
Br	1.96	574	2.24	537
I	2.20	836	1.53	784
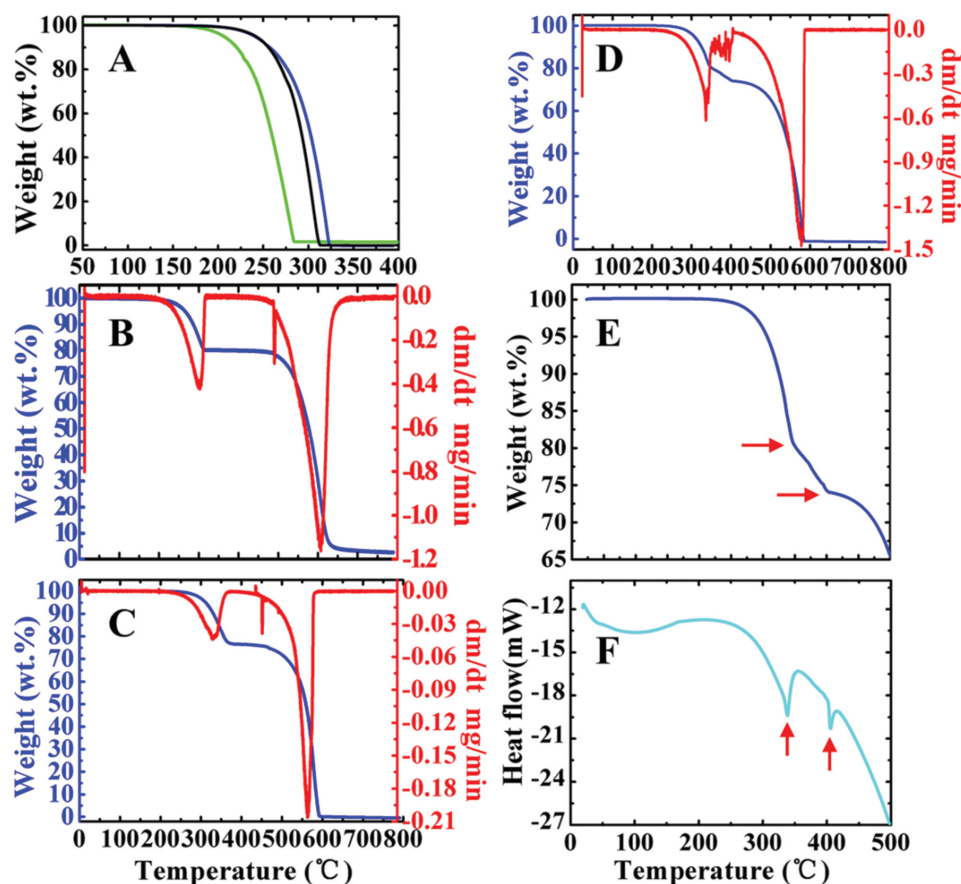
Figure 6. The thermal stability of the samples. A) TGA curves of individual organic components, CH_3NH_3X (X = Cl, Br, I); B,C) and D) TGA curves and corresponding first derivatives for the $CH_3NH_3PbX_3$ (X = Cl, Br, I) perovskite powders; E) zoomed version of (A) to identify accurate temperatures; F) DSC heating curve of the region for organic component.

measurements of the starting materials CH_3NH_3X (X = Cl, Br, I) are also presented. The organic components, CH_3NH_3Cl, CH_3NH_3Br, and CH_3NH_3I, undergo 100% weight loss in a single step, with the onset temperatures at 171 °C, 202 °C, and 202 °C (Figure 6A) respectively, suggesting clear sublimation without complex decomposition for these materials. However, the perovskite products seem to be more stable at high temperature, showing no change up to 214 °C for X = Cl (Figure 6B), and up to 257 °C for X = Br (Figure 6C), respectively. The organic components CH_3NH_3X (X = Cl, Br) appear to be stabilized in the perovskite structure for there is no weight loss at their respective sublimation temperatures.

On the other hand, a different thermal behavior is observed in $CH_3NH_3PbI_3$ as both TGA (Figure 6E) and DSC (Figure 6F) curves show two thermal events occurring in temperature range from 30 °C to 500 °C. The material first undergoes 20% mass loss of HI at 240 °C, followed by 6% loss of the CH_3NH_2 component at 337 °C, indicating that the amine group is bound into the perovskite matrix more tightly than HI. It should be noted that this decomposition, by sequential loss of HI followed by the CH_3NH_2, was not detected for the pure CH_3NH_3I compound (Figure 6A), showing that this decomposition behavior occurs only when the organic species is incorporated into the perovskite structure.[31] All pure organic component materials

CH_3NH_3X (X = Cl, Br, I) are sublimed in a single mass-loss step at a well-defined temperature.

Comparing to the well-studied thin film version of the $CH_3NH_3PbI_3$ material that decomposes around 150 °C,[32,33] the single crystals appear to be more stable, for no signature of thermal decomposition is observed until 240 °C.

To investigate the trap density (n_{trap}) in the single-crystalline $CH_3NH_3PbX_3$ (X = Br, I) materials, hole-only and electron-only devices, as shown in Figure S4 (Supporting Information), were fabricated and characterized using a dark I–V technique. **Figure 7** displays a kink in the dark I–V curve for both devices. When the applied voltage is lower than the kink-point voltage, the current I increases linearly as V, indicating an Ohmic response. As it goes beyond the kink-point voltage, the current I exhibits a quick non-linear increase, indicating that the trap states are fully filled by the injected carriers. The applied voltage at the kink point is known as the trap-filled limit voltage V_{TFL}, determined by the trap density:[34]

$$V_{TFL} = \frac{en_{trap}L^2}{2\varepsilon_0\varepsilon} \tag{1}$$

where L is the thickness of the perovskite single crystals, ε is the relative dielectric constant for $CH_3NH_3PbX_3$ (X = Br, I) and ε_0 is

COMMUNICATION
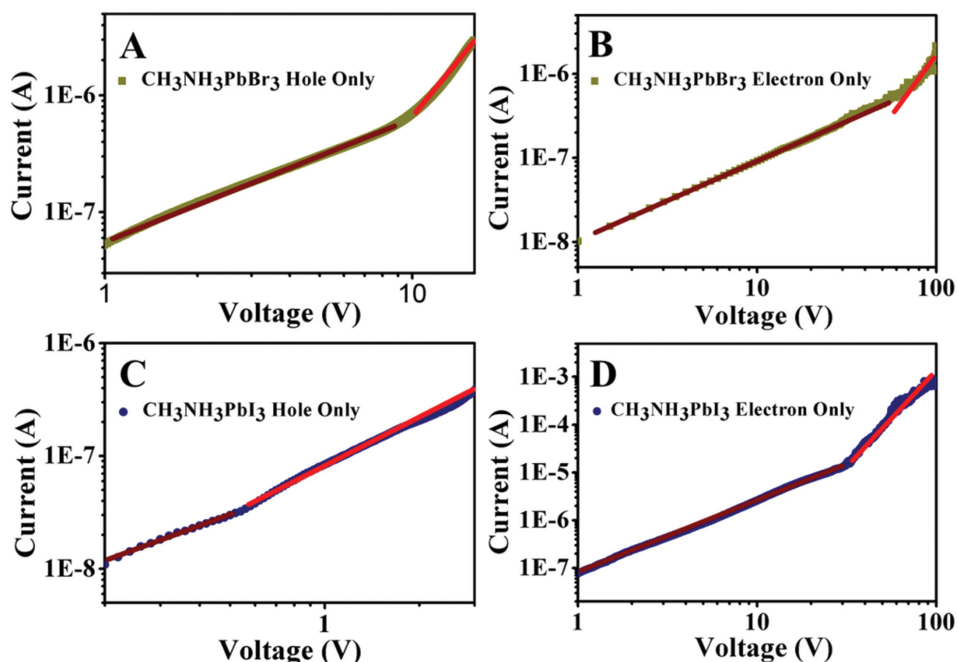
Figure 7. Current–voltage traces and trap-density characterization of single-crystalline $CH_3NH_3PbX_3$ (X = Br, I). A,B) Current–voltage curve for a hole-only $CH_3NH_3PbBr_3$ device and an electron-only $CH_3NH_3PbBr_3$ device; C,D) Current–voltage curve for a hole-only $CH_3NH_3PbI_3$ device and an electron-only $CH_3NH_3PbI_3$ device.

the vacuum permittivity. Hence the trap density n_{trap} can be calculated using Equation 1. Based on Figure 7A,C, the V_{TFL} values for $CH_3NH_3PbBr_3$ and $CH_3NH_3PbI_3$ are 9.20 and 0.56 V, respectively. The corresponding hole trap density is 2.6×10^{10} cm^{-3} for $CH_3NH_3PbBr_3$ and 1.8×10^9 cm^{-3} for $CH_3NH_3PbI_3$. Using the same procedure, the electron trap densities are determined for $CH_3NH_3PbBr_3$ (Figure 7B) and $CH_3NH_3PbI_3$ (Figure 7D) to be 1.1×10^{11} cm^{-3} and 4.8×10^{10} cm^{-3} respectively. Note that this is the first report on the electron trap density measured for the $CH_3NH_3PbBr_3$. For $CH_3NH_3PbI_3$, the present larger crystal size appears to show a hole trap density about 20 times smaller than the previous reports measured using smaller crystals,[7,8] likely due to larger single crystals grown with better quality. When compared to the established inorganic semiconductors, including Si (n_{traps} = 10^{13}–10^{14} cm^{-3}),[35,36] CdTe (n_{traps} = 10^{11}–10^{13} cm^{-3}),[37] CIGS ($n_{traps} \approx 10^{13}$ cm^{-3}),[38] etc., it is surprising to see that the perovskites show significantly fewer trap states.

The Hall effect is another key measurement for the semiconductor quality. It is found that the single-crystalline $CH_3NH_3PbI_3$ shows a very low hole concentration of 8.8×10^{11} cm^{-3} and a high carrier mobility of 34 cm^2 V^{-1} s^{-1}; the crystalline $CH_3NH_3PbCl_3$ gives an even lower number in electron concentration, 5.1×10^9 cm^{-3}, while its carrier mobility is even higher at 179 cm^2 V^{-1} s^{-1}. In comparison, these two numbers for the $CH_3NH_3PbBr_3$ appear to be moderate, with a hole concentration of 3.87×10^{12} cm^{-3} and carrier mobility of 4.36 cm^2 V^{-1} s^{-1}.

Based on the above superior properties in the defect state density, carrier concentration, and mobility, it is expected that the present single-crystalline perovskites are promising for a new generation of high-performance optoelectronic applications.

In summary, we have grown large, single-crystalline $CH_3NH_3PbX_3$ (X = Cl, Br, I) perovskites using a facile solution method. The powder XRD analyses confirm the formation at room temperature, of a tetragonal structure (space group $I4/m$) for X = I, a cubic structure (space group $Pm\overline{3}m$) for X = Br, and a cubic structure (space group $Pm\overline{3}m$) for X = Cl, respectively. Optical-absorption measurements reveal that all three perovskite crystals show broader absorption, compared to their microcrystalline counterparts, as demonstrated by their reduced optical bandgaps. In addition, we have observed the PL emission at 402 nm from $CH_3NH_3PbCl_3$ for the first time. The low trap density and high carrier mobility indicate that the present large, single-crystalline $CH_3NH_3PbX_3$ (X = Cl, Br, I) is a promising material for high-performance optoelectronic devices. Both the TGA and the DSC show that the large $CH_3NH_3PbI_3$ crystals are more stable at much higher temperature compared to their thin-film material counterpart.

As the large, single-crystalline material is the fundamental basis for the semiconductor, electronics, and optoelectronic industries, it is expected that this technique will bring large perovskite crystals into the market and their availability will, in turn, revolutionize broad applications of the high-quality single-crystalline products in photovoltaics, optoelectronics, lasers, photodetectors, and LEDs, etc.

Experimental Section

The powder XRD patterns were collected using a Rigaku (Smartlab-9kW) X-ray diffractometer equipped with a Cu K$_\alpha$ X-ray (λ = 1.54186 Å) tubes. TGA was performed on a TA SDT-Q600 V20.9 (Build 20). UV–vis–NIR diffuse reflectance spectroscopy was measured at room temperature using a UV–vis–NIR spectrophotometer (Perkin–Elmer Lambda 950). PL

measurements of bulk crystals were performed with a Renishaw inVia Raman microscope. The Hall effect was characterized using a Lake Shore Hall test system 7700A. *I–V* measurements were made using a Keithley 2400 instrument.

Supporting Information

Supporting Information is available from the Wiley Online Library or from the author.

Acknowledgements

[1] Best Research-Cell Efficiencies, NREL, www.nrel.gov/ncpv/images/efficiency_chart.jpg; accessed: July 2015.

[2] S. D. Stranks, G. E. Eperon, G. Grancini, C. Menelaou, M. J. P. Alcocer, T. Leijtens, L. M. Herz, A. Petrozza, H. J. Snaith, *Science* **2013**, *342*, 341.

[3] G. Xing, N. Mathews, S. Sun, S. S. Lim, Y. M. Lam, M. Grätzel, S. Mhaisalkar, T. C. Sum, *Science* **2013**, *342*, 344.

[4] G. J. Wetzelaer, M. Scheepers, A. M. Sempere, C. Momblona, J. Avila, H. J. Bolink, *Adv. Mater.* **2015**, *27*, 1837.

[5] A. Y. Mei, X. Li, L. F. Liu, Z. L. Ku, T. F. Liu, Y. G. Rong, M. Xu, M. Hu, J. Z. Chen, Y. Yang, M. Grätzel, H. W. Han, *Science* **2014**, *345*, 295.

[6] Y. Shao, Z. Xiao, C. Bi, Y. Yuan, J. Huang, *Nat. Commun.* **2014**, *5*, 5784.

[7] Q. F. Dong, Y. Fang, Y. Shao, P. Mulligan, J. Qiu, L. Cao, J. S. Huang, *Science* **2015**, *347*, 967.

[8] D. Shi, V. Adinolfi, R. Comin, M. Yuan, E. Alarousu, A. Buin, Y. Chen, S. Hoogland, A. Rothenberger, K. Katsiev, Y. Losovyj, X. Zhang, P. A. Dowben, O. F. Mohammed, E. H. Sargent, O. M. Bakr, *Science* **2015**, *347*, 519.

[9] Y. Y. Dang, Y. Liu, Y. X. Sun, D. S. Yuan, X. L. Liu, W. Q. Lu, G. F. Liu, H. B. Xia, X. T. Tao, *CrystEngComm* **2015**, *17*, 665.

[10] T. Baikie, Y. N. Fang, J. M. Kadro, M. Schreyer, F. X. Wei, S. G. Mhaisalkar, M. Grätzel, T. J. White, *J. Mater. Chem. A* **2013**, *1*, 5628.

[11] A. Maalej, Y. Abid, A. Kallel, A. Daoud, A. Lautié, F. Romain, *Solid State Commun.* **1997**, *103*, 279.

[12] A. Maalej, M. Bahri, Y. Abid, N. Jaïdane, *Can. J. Phys.* **1999**, *77*, 717.

[13] A. Poglitsch, D. Weber, *J. Chem. Phys.* **1987**, *87*, 6373.

[14] N. Onoda-Yamamuro, T. Matsuo, H. Suga, *J. Phys. Chem. Solids* **1990**, *51*, 1383.

[15] H. Mashiyama, Y. Kawamura, E. Magome, Y. Kubota, *J. Kor. Phys. Soc.* **2003**, *42*, S1026.

[16] Y. Kawamura, H. Mashiyama, K. Hasebe, *J. Phys. Soc.* **2002**, *71*, 1694.

[17] L. Chi, I. Swainson, L. Cranswicka, J. H. Her, P. Stephens, O. Knop, *J. Solid State Chem.* **2005**, *178*, 1376.

[18] N. Preda, L. Mihut, M. Baibarac, I. Baltog, R. Ramer, J. Pandele, C. Andronescu, V. Fruth, *J. Mater. Sci.: Mater. Electron.* **2009**, *20*, 465.

[19] E. Edri, S. Kirmayer, M. Kulbak, G. Hodes, D. Cahen, *J. Phys. Chem. Lett.* **2014**, *5*, 429.

[20] Y. P. Fu, F. Meng, M. B. Rowley, B. J. Thompson, M. J. Shearer, D. W. Ma, R. J. Hamers, J. C. Wright, S. Jin, *J. Am. Chem. Soc.* **2015**, *137*, 5810.

[21] K. N. Liang, D. B. Mitzi, M. T. Prikas, *Chem. Mater.* **1998**, *10*, 403.

[22] C. C. Stoumpos, C. D. Malliakas, M. G. Kanatzidis, *Inorg. Chem.* **2013**, *52*, 9019.

[23] S. Tsunekawa, T. Fukuda, A. Kasuya, *J. Appl. Phys.* **2000**, *87*, 1318.

[24] R. E. Wasylishen, O. Knop, J. B. Macdonald, *Solid State Commun.* **1985**, *56*, 581.

[25] R. D. Shannon, *Acta Crystallogr.* **1976**, *A32*, 751.

[26] L. Dimesso, M. Dimamay, M. Hamburger, W. Jaegermann, *Chem. Mater.* **2014**, *26*, 6762.

[27] N. Kitazawa, Y. Watanabe, Y. Nakamura. *J. Mater. Res.* **2002**, *37*, 3585.

[28] A. Kojima, K. Teshima, Y. Shirai, T. Miyasaka, *J. Am. Chem. Soc.* **2009**, *131*, 6050.

[29] Y. X. Zhao, A. Nardes, K. Zhu, *Faraday Discuss.* **2014**, *170*, 301.

[30] S. D. Wolf, J. Holovsky, S. J. Moon, P. Löper, B. Niesen, M. Lsdinsky, F. J. Hang, J. H. Yum, C. Ballif, *J. Phy. Chem. Lett.* **2014**, *5*, 1035.

[31] A. Dualeh, P. Gao, S. I. Seok, M. K. Nazeeruddin, M. Grätzel, *Chem. Mater.* **2014**, *26*, 6160.

[32] T. Supasai, N. Rujisamphan, K. Ullrich, A. Chemseddine, Th. Dittrich, *Appl. Phys. Lett.* **2013**, *103*, 183906.

[33] A. Dualeh, T. Moehl, N. Tétreault, J. Teuscher, P. Gao, M. K. Nazeeruddin, M. Grätzel, *Adv. Funct. Mater.* **2014**, *24*, 3250.

[34] R. H. Bube, *J. Appl. Phys.* **1962**, *33*, 1733.

[35] J. R. Ayres, *J. Appl. Phys.* **1993**, *74*, 1787.

[36] I. Capan, V. Borjanović, B. Pivac, *Sol. Energy Mater. Sol. Cells* **2007**, *91*, 931.

[37] A. Balcioglu, R. K. Ahrenkiel, F. Hasoon, *J. Appl. Phys.* **2000**, *88*, 7175.

[38] L. L. Kerr, S. S. Li, S. W. Johnston, T. J. Anderson, O. D. Crisalle, W. K. Kim, J. Abushama, R. N. Noufi, *Solid State Electron.* **2004**, *48*, 1579.